Meas. Sci. Technol. 27 (2016) 025005 (13pp) doi:10.1088/0957-0233/27/2/025005

Empirical compensation of reciprocity failure and integration time nonlinearity in a mid-wave infrared camera

I Romm, M Lev and B Cukurel

Turbomachinery & Heat Transfer Laboratory, Faculty of Aerospace Engineering, Technion–Israel Institute of Technology, Haifa 3200012, Israel

E-mail: beni@cukurel.org

Received 19 August 2015, revised 1 November 2015
Accepted for publication 16 November 2015
Published 29 December 2015

Abstract

Thermal-infrared radiation measurements, conducted using an InSb camera, indicated a failure of the reciprocity law for a wide range of radiation intensities and integration times. When reciprocity between radiation flux and integration time was assumed, the radiation estimates, computed from different combinations of output signals and selected integration time values, suffered from imprecisions of up to 12%. Temperature errors of ~4% were predicted for low emissivity surfaces, at all temperatures. A novel empirical methodology, which compensates for multiple nonlinearity effects, is presented. Among different types of models, it is demonstrated that an equation, which represents a power-law dependence of the output signal on integration time best describes the physical system. Experimental procedures are suggested to avoid nonlinearity-related errors.

Keywords: infrared camera, infrared imaging, reciprocity failure, InSb FPA, multi-integration time radiometry, extended dynamic range, integration time nonlinearity

(Some figures may appear in colour only in the online journal)

Nomenclature

A_i	fitting parameters
c_1	1st radiation constant
c_2	2nd radiation constant
CWL	central wavelength
DL	digital level
$\mathrm{DL_M}$	measured DL
$\mathrm{DL_P}$	predicted DL
FWHM	full-width, half-maximum
GOF	goodness-of-fit
IR	infrared
IT	integration time
k	dataset index
MWIR	mid-wave IR
NTE	nonlinearity of total exposure.
P	Schwarzschild's coefficient
R	radiation flux
RMSE	root mean square error
SNR	signal-to-noise ratio
SSE	sum of squared errors
t	temperature (°C)
T	temperature (K)
ε	emissivity
λ	wavelength

1. Introduction

Many industrial and scientific applications require the accurate measurement of radiation flux emitted by target surfaces. One of the most important applications is thermal *infrared* (IR) imaging for non-contact measurement and monitoring of *temperature* (T). Using IR cameras allows to obtain not only the local temperature (as can be done with IR pyrometers), but also the 2D temperature distributions on a surface.

A common assumption in digital radiometry is reciprocity between *radiation flux* (R) and *integration time* (IT), analogous

0957-0233/16/025005+13$33.00

to 'exposure duration' used in chemical photography. The reciprocity law states that for a given optical system, all combinations of R and IT are equivalent as long as their product (termed *total exposure*) remains constant [1, 2]:

$$DL = R \cdot IT, \tag{1}$$

where DL (*digital level*) expresses total exposure in arbitrary units directly output by the camera detector. As with other detectors that produce a digital signal, these DL values are tied to the detector's dynamic range, which is limited by the random noise at low signal levels and by saturation at high levels. Hence, only R that result in a DL within the dynamic range are measurable.

The reciprocity law, (1), is sometimes used to compare R obtained from images taken at different IT. The assumption of proportionality between DL and IT is of paramount importance when a photographed scene contains sources with large R differences, due to differing object temperatures, emissivities and view factors. In that case, the span of R may exceed the dynamic range of the detector, thus limiting the ability to capture some radiations. To overcome the difficulty inherent to a large intensity span, the responsivity of a detector may be adjusted by varying IT, which in turn "shifts" the measurable R range. A common practice in radiometry involves the acquisition of several frames with varying IT to achieve an extended dynamic range.

Figure 1 demonstrates the viability of manipulating a detector's dynamic range via the choice of IT. Namely, increasing IT allows discerning R previously found below the noise level. A higher-sensitivity detector is able to measure weaker radiations at an acceptable signal-to-noise ratio (SNR), but on the other hand, it saturates for a lower radiation. Conversely, at a shorter IT, the dynamic range shifts to higher flux levels—thus allowing to measure previously saturated signals. Moreover, figure 1 further portrays how detector readings which were previously considered unacceptable due to either saturation or low SNR (red circles) fall into the valid range following an appropriate choice of IT (green squares which are vertically aligned with the red circles). Overall, combining data from several images, acquired with different IT, allows measuring a broad range of R using a single detector. This photographic technique is commonly known as *high-dynamic-range imaging* (HDR).

Reciprocity is said to 'fail' whenever the proportionality defined in equation (1) does not hold. In reality, this is actually the nonlinearity of total exposure. The present work distinguishes between two related yet distinct effects that result in the *nonlinearity of total exposure* (NTE): integration time nonlinearity and reciprocity failure. Integration nonlinearity is the deviation of the output signal from a straight line, when observing a constant radiation flux at different exposure times. On the other hand, reciprocity failure is the deviation from a constant integrated signal (DL) when varying the flux and inversely adapting the exposure time.

In the field of chemical photography, the first cases of NTE (and historically referred to as 'reciprocity failure') in photosensitive materials were documented over a century ago [1, 2]. According to these observations, a nonlinear dependence of the material's response (represented by DL) on the exposure time (represented by IT) was found. A correction that accounts for this effect was introduced into equation (1), and the subsequent equation characterizing total exposure became:

$$DL = R \cdot IT^{P}. \tag{2}$$

The parameter P in equation (2) is Schwarzschild's coefficient, and is generally close to unity. When $P = 1$, equation (2) is equivalent to equation (1), which signifies that NTE does not exist. When $P \neq 1$, DL no longer depends on $R \cdot IT$ as a whole, but on R and IT individually. Nowadays, the effect where the law of reciprocity breaks down at extreme values of R or IT is well known in chemical photography. A similar phenomenon was observed in the visible and near-infrared wavelength range, using a photodetector equipped with HgCdTe semiconductor array [3, 4].

The exact mechanism responsible for NTE in semiconductors remains inadequately understood. To compile a non-exhaustive list of its causes, it is useful to consider literature explicitly related to both integration nonlinearity and reciprocity failure. Integration time nonlinearity may be associated with various factors, such as: charge leakage during the readout phase due to pixel irradiation, supraresponsivity, saturation and anti-blooming, electronic transformations from photoelectrons to digital units, etc [5]. On the other hand, causes for reciprocity failure include: bias voltage that is applied to a pixel node diode junction which affects the junction's capacitance and hence the apparent flux [4]; image persistence due to the slow release of trapped charge in the bulk material [6] or the fact irradiation is not being blocked during the readout phase, which causes the leakage of a significant amount of electrons.

The assumption that pixel response is proportional to irradiation is very deeply rooted in the scientific community, to the extent that it is implied. A prominent example of this is the widely practiced NUC procedure [7, 8]. In NUC, it is assumed that non-uniformity between pixels manifests in bias and slope differences on a per-pixel basis, and NUC corrects for this by mathematically bringing all pixels to a common linear response curve. Two methods exists for NUC, using: (a) two or more highly uniform radiation sources of different magnitude (b) two or more acquisition IT of the same radiation source. In reality, both approaches ignore the nonlinearity of total exposure within each pixel, caused by reciprocity failure and integration time nonlinearity respectively. This approach may be a sufficient approximation for cases when the two integrated signals are close with regard to the amount of nonlinearity the system exhibits. However, in HDR scenarios, implementation of NUC might cause more harm than good, since the intermediate radiations will be underpredicted due to the concaveness of the true response curve.

2. Motivation

In an attempt to acquire accurate local temperature readings on a surface of varying radiance, measurements were carried out using a digital camera sensitive to *mid-wave IR* (MWIR) radiation. As typically accepted within the community [9, 10],

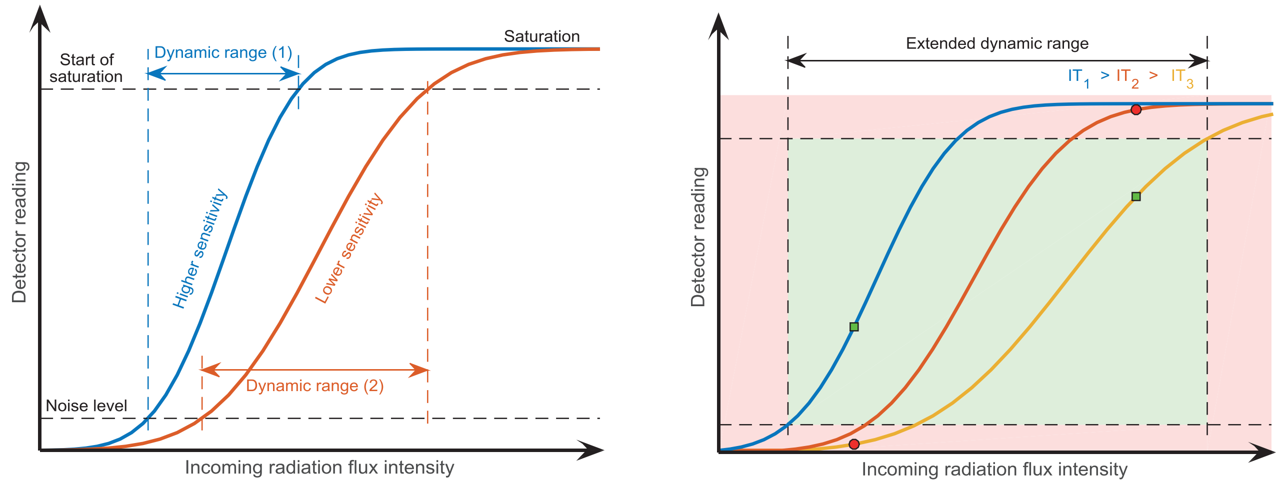

Figure 1. Manipulation of a detector's dynamic range via the choice of IT. Left: comparison of the dynamic ranges of a high and a low sensitivity detector: the higher-sensitivity detector is able to measure weaker radiations at an acceptable *signal-to-noise ratio* (SNR), but saturates for a lower radiation. Right: dynamic range extension via the variation of IT: detector readings that fall within the red-tinted (outer) regions are considered unreliable due to either saturation or low SNR (such measurements are shown as red circles). Using an appropriate choice of IT, the detector's response curve can be shifted such that a measurement of *R* becomes valid (shown as green squares, vertically aligned with the red circles).

initial radiation flux estimates assumed that the recorded signal was proportional to both integration time and irradiance. However, when different combinations of digital level and integration time were tested, the thermometric results were found to suffer from unexpectedly low precision.

Literature documenting NTE (reciprocity failure and integration nonlinearity) in semiconductor IR cameras is scarce; its effect not sufficiently quantified, perhaps underestimated, and thus often neglected altogether. Furthermore, according to our best knowledge, no systematic method, which alleviates this issue, was prior documented.

In light of the insufficient precision associated with accepted radiometry practices, the aim of the present research effort is to obtain an accurate and consistent estimate of the normalized incident radiation flux. Therefore, the experimental investigation quantifies the error associated with nonlinearity of total exposure in MWIR radiometry, explores its implications on temperature estimates, and provides an empirical model to compensate for this effect. The ultimate goal is to negate the error introduced by the selection of integration time for readings within the system's extended dynamic range.

3. Experimental setup and procedure

IR radiation measurement was conducted using a FLIR SC7600 MWIR camera with an InSb focal plane array. The camera was equipped with three narrow bandpass filters (with *central wavelengths* (CWL) at 3.45 μm, 3.63 μm, and 3.78 μm) within the atmospheric window of 3–4 μm range. The objects were viewed through the FLIR ATS L0118 lens. Further details about the elements on the optical path can be found in table 1. Other than the detector, lens and filters, no additional absorptive components or effects were considered. The spectral transmission of the lens and the used filters, as well as the response curve of the detector, are presented in figure 2. The lens transmittance is close to 100% over the ranges of filter transmissions. The maximum transmission levels of the filters are about 90%. Two of the three filters have a spectral transmission width of 0.14 μm (FWHM), whereas the width of the 3.78 μm filter is 0.04 μm (FWHM). The responsivity of the detector is increasing with wavelength. The calibration of the optical system's response to radiation was conducted using a commercial blackbody of type CALSYS-1200-BB, operational up to 1200 °C. The desired temperatures are set in the blackbody controller, which operates based on the feedback loop of a NIST traceable R-type thermocouple in contact with the cavity wall. The blackbody radiation source enabled obtaining datasets of DL with different *IT* and different radiation levels (determined by the blackbody cavity temperature).

Representative of common industrial/laboratory needs, the experimental setup consisted of a solid rod made of aluminum alloy 2024-T351. A 3 mm bore was drilled to a depth of 30 mm in the center of the front surface—a cavity acting as high emissivity reference radiation source. The rod was placed inside a Carbolite MTF 12/38/250 tube furnace, such that its front surfaces on both sides are slightly protruding into the ambient air, as shown in figure 3.

During experiments, the rod was heated to a steady temperature; the high conductivity of the metal, along with its large thermal inertia, ensured isothermicity at all points of the body within 0.15 °C. *R* was then measured through IR imaging of the rod's front surface at 8 separate *IT*s.

A *dark frame,* a frame captured while an object of constant emissivity at ambient temperature obscures the lens, was acquired alongside every image-of-interest. During post-processing, dark frames were subtracted from the corresponding images-of-interest to reduce *fixed-pattern noise* (FPN) and as a replacement for the *non-uniformity correction* (NUC) [11]. The effectiveness of this technique was guaranteed as long as measurement frames and dark frames were taken in close succession [12]. To reduce detector noise, depending upon the data set, each recorded image consisted of the average of 180–500

Table 1. Summary of the optical equipment.

Item Type	Manufacturer + Model	Additional Information
MWIR Camera	FLIR SC7600	Focal plane array (FPA) material: Indium-antimonide (InSb). FPA temperature: 76 K, cooled by a Stirling cooler. FPA resolution: 640 × 512 pixels with 15 × 15 μm pixel size. FPA sensitivity band: 1.0–6.0 μm. A/D resolution: 14-bit.
Lens	FLIR ATS L0118	MW, $f = 100$ mm, $F\# = 2$.
Optical filters	EO BP IR 3.46UM X 140NM EO BP IR 3.60UM X 140NM SP NB-3800-040 25.4 mm × 1 mm	EO—Edmund Optics, SP—Spectrogon. Note: a slight discrepancy exists between the declared filter CWL and the CWL computed from the published shape. This work uses the latter.

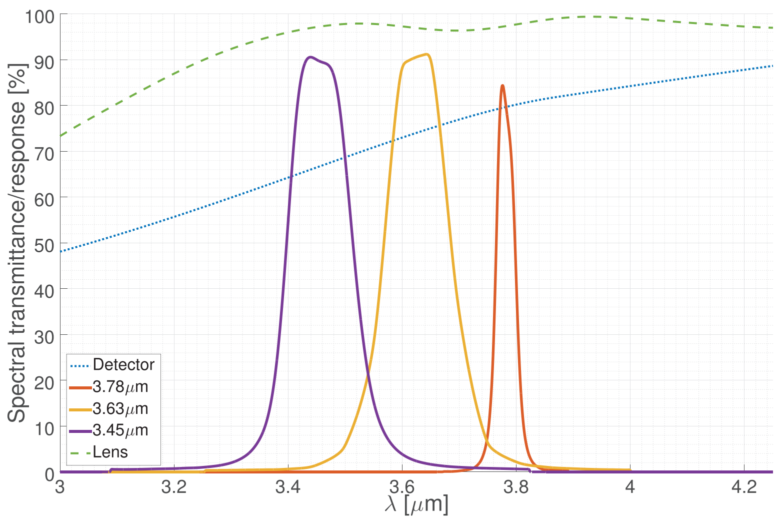

Figure 2. The transmittance (filters, lens) and response (detector) of the optical elements employed in this study.

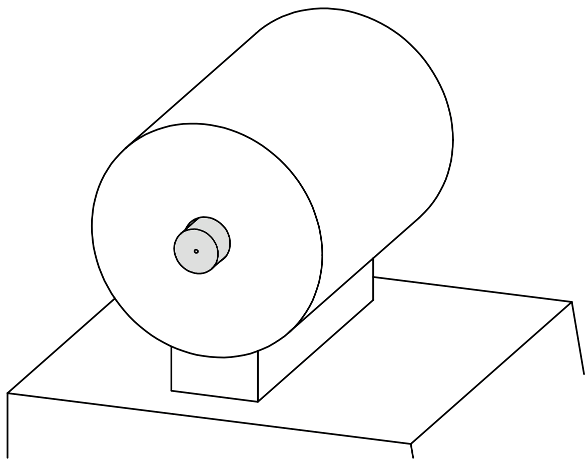

Figure 3. Schematic of the experimental setup: an aluminum rod with a bore is placed within a tube furnace, which is subsequently heated.

frames. According to the camera manufacturer, even 100 frames sufficed to 'eliminate virtually all time noise' [13].

Figure 4 presents a sample image taken during the experiment, showing the differences in *DL* between the polished aluminum and the cavity regions. In our typical experimental conditions, the cavity's radiation was ~10 times higher than that of the polished surface (the emissivity of polished aluminum is $\varepsilon < 0.1$). *IT* was varied such that resulting *DL* of the high-emissivity region was within the manufacturer-declared range of *DL* linearity versus the incoming *R* [14]. The maximum temperature difference between the regions was estimated to be within 1.5 °C.

4. Experimental results

For the validity testing of the reciprocity assumption, images of the same scene were captured intentionally at several *IT*. For each image, the representative *DL* of each region was chosen as the mean *DL* within the areas delimited by the dashed circle and rectangle in figure 4, representing the cavity and the polished regions, respectively. *R* was then estimated using equation (1) and *R* versus *IT* were charted in figure 5 (black dots). Since the temperature of the rod was constant throughout the experiment, the apparent *R* was expected to be constant as well, and all dots were supposed to lie on a horizontal line. Counterintuitively, values of *R* were distinctly different and dependent on the selection of camera *IT*, in spite of a constant radiance emanating from the source. The deviation was not random and a systematic error trend was clearly present. Assuming reciprocity implied characterizing all of the different apparent *R* using a single value (typically obtained by linear regression with equation (1)), despite the clearly sloped nature of the data. Thus, figure 5 evidenced that the estimation of *R* under the reciprocity assumption could not be valid.

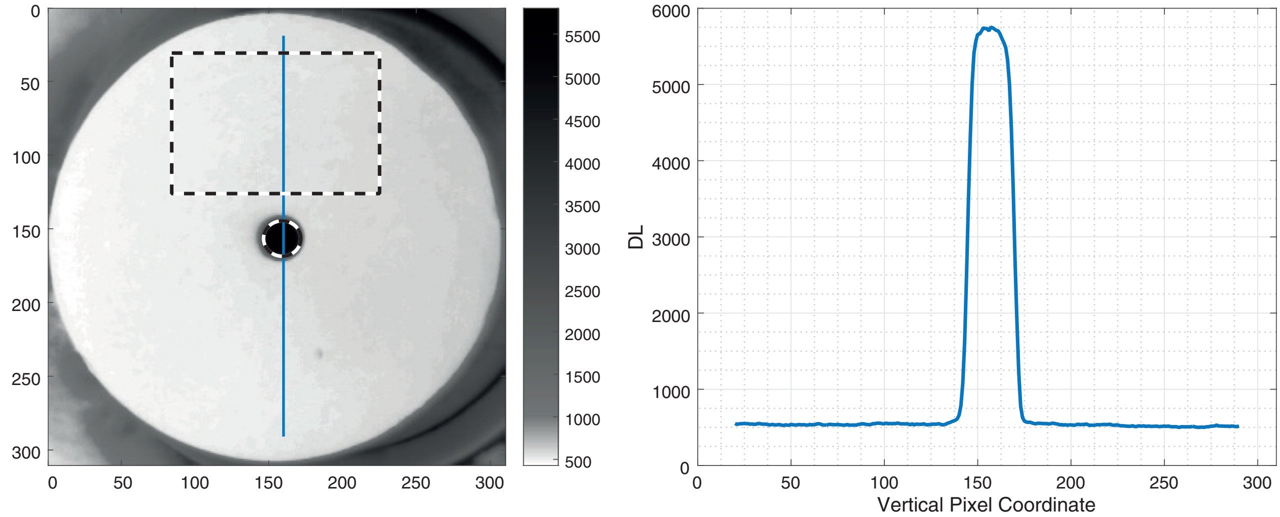

Figure 4. Example DL image of the rod's front surface at $IT = 1200\ \mu$s. Left: a photograph showing the cavity as a dark circle (i.e. a strongly emissive region of the photo) in the center, surrounded by brighter (i.e. less emissive), polished aluminum. The representative DL value of each region was chosen as the mean *DL* within the areas delimited by a dashed circle and rectangle, representing the cavity and the polished regions, respectively. Right: DL readings along the vertical centerline.

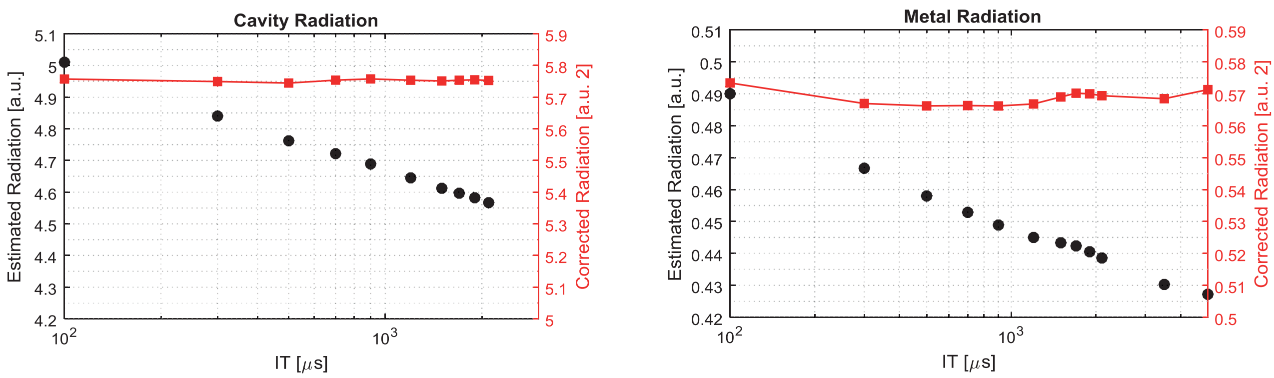

Figure 5. Incident radiation flux estimates for the cavity and the metal, showing the effect of integration time nonlinearity. Black dots show the radiation estimates obtained by the ratio DL/IT, which is seen to depend on the choice of *IT*. Red squares represent the same data after nonlinearity compensation.

To further illustrate the imprecision introduced by the reciprocity assumption, the system's expected output signal was predicted for different combinations of *IT* with the single characteristic *R*, and compared with the measured signal. The normalized residual between the measured and predicted *DL* values (DL_M, DL_P), which is indicative of the radiation estimate error, was charted in figure 6. In the high emissivity region, the deviations from the predicted levels were up to 8%, whereas the low emissivity zone suffered from imprecisions of up to 12%. With respect to the chosen camera *IT*, there appeared to be a power law dependence that characterized the deviation from the fit.

5. Multi-integration time camera calibration

A traditional calibration procedure of *R* versus *T*, which assumes reciprocity, is usually conducted with a single *DL* reading at every temperature, since the radiation estimate is thought not to be dependent on the choice of *IT*. *DL/IT* data points obtained at several exemplary calibration conditions for the 3.45 μm CWL filter, are charted in figure 7. At each constant temperature, although the radiation of the blackbody is invariant, the evident deviation from a horizontal line is observed for a broad range of temperatures (or source radiances). Similar decreasing trends are also encountered for the other optical filters.

To obtain an empirical equation that can model the true system response, a multi-variable calibration needs to be performed. Since a nonlinear dependence of *DL* on *IT* is known to exist, an alternate calibration strategy is considered, which entails measurements at multiple *IT* for every temperature. This experimental procedure allows to study the dependence of the camera's output signal (*DL*) on *R* and *IT* independently. As presented in figure 8, the (*IT, T, DL*) data points constitute the optical system response to 54 different temperatures of the blackbody, from 80 °C to 712 °C. Each temperature is sampled at eight *IT*, such that the largest of which results in *DL* of ~11 000 (before background subtraction). This ensures that the detector remains far from saturation. The other *IT* s are temporal fractions of $\mathrm{IT}_{\mathrm{DL}} = {}_{11000}$, differing by 12.5% (i.e. 7/8, 6/8 etc).

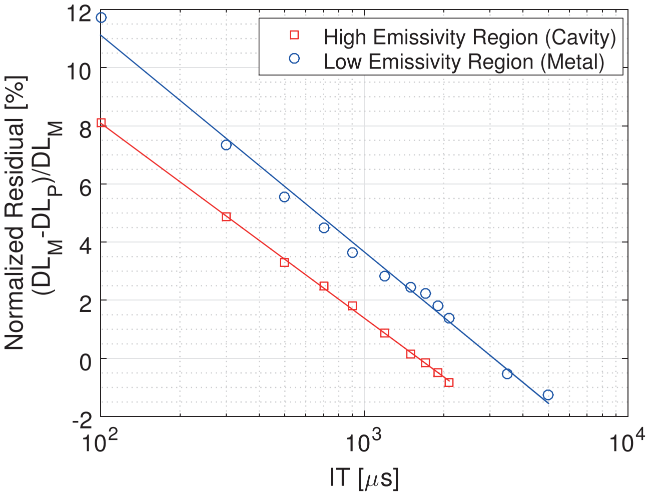

Figure 6. Residual between a predicted curve and unsaturated experimental data points taken at different IT for a constant radiation under the reciprocity assumption (3.45 μm CWL filter).

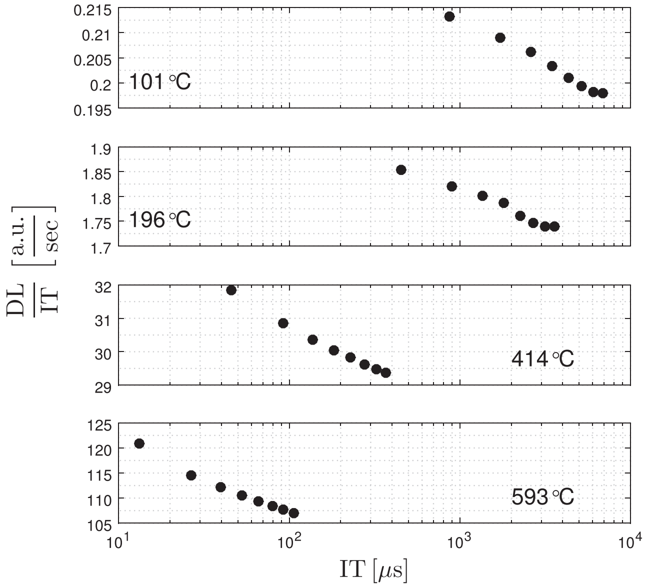

Figure 7. Examples of data points obtained in the calibration procedure at different temperatures using the 3.45 μm CWL filter. The apparent radiation, estimated by DL/IT, seems to be dependent on the selection of camera IT, despite the source temperature (and therefore the radiation flux) being constant.

6. Compensating the nonlinearity of total exposure

In order to compensate for NTE, an equation able to tie accurately measured DL with different combinations of R and IT is needed. To find R, the source radiation is derived from a known temperature of a blackbody for a known optical path. The principal behind this method is the calibration of the detected signal against well-defined radiations, related to the blackbody's temperature via the Planck equation:

$$B_\lambda(\lambda, T) = \frac{c_1}{\lambda^5}\frac{1}{\exp(c_2/\lambda T) - 1}, \tag{3}$$

where c_1, c_2, T, λ are the 1st and 2nd radiation constants, temperature and wavelength, respectively. However, equation (3) cannot be used directly, as the detected radiation constitutes but a limited part of the incoming blackbody irradiation. The optical elements have a wavelength-dependent transmittance (associated with the finite spectral width of the filter and the transmission of the lens), and the quantum efficiency of the detector is uneven. Therefore, the camera is calibrated to enable determining an accurate quantitative relation between its output and incident radiation. The calibration curve used in radiometry mimics Planck's formula (3), relying on the adjustable parameters A, B and C, which take into account the detector response, the spectral transmittance of the optical drivetrain and the form factor in the experiment [15]:

$$R(T; \lambda) = \frac{A}{\exp(B/T) + C}. \tag{4}$$

Equation (4) prescribes the changes of R with respect to T. The parameters A, B and C are found during the fitting process separately for every optical configuration. Thus, at known source temperatures, and for a well-characterized system, T can fully represent R. Thereby, DL can be considered as a function of T and IT, all three of which are readily available during controlled experiments. These resulting data points (IT, T, DL) can then be fitted with different equations, intended to replace the reciprocity law. The considered equations are separated into two distinct groups:

The 1st group of equations consists of generalizations of Schwarzschild's law found in equation (2). It implies that the parameter P, which is constant in equation (2), may be replaced by a function of the radiation flux transmitted by the optical system—$P(R)$:

$$DL = R \cdot IT^{P(R)}. \tag{5}$$

It should be noted that if the radiation is invariant within a dataset k, the function $P(R_k)$ becomes a constant value, P_k. Furthermore, data need not belong to a constant temperature/radiation dataset in order to obtain equation coefficients, the only constraint being a sufficient amount of data points as dictated by the chosen model for $P(R)$.

Data used in this analysis included P and R values that were found by fitting equation (2) to every distinct-radiation dataset obtained by varying IT, at each of the constant source temperatures. For each distinct-radiation dataset, $P = P_k$ was some constant value obtained independently for every temperature T_k. Characterizing the power P_k found in all datasets yielded a representation of P as the function of R, as shown by black dots in figure 9. The R scales for each filter are consistent within themselves, however vary from one another due to differences in integral transmission between the optical configurations. Comparing the different models that fit the experimental data enabled quantifying the effectiveness of a multitude of possible relations between P and R in representing the nonlinear dependence of DL on R and IT.

The simplest models for the power $P(R)$ in equation (5) were linear or quadratic functions in R, as shown in the following equations:

$$P(R) = A_0 + A_1 R \tag{6}$$

$$P(R) = A_0 + A_1 R + A_2 R^2. \tag{7}$$

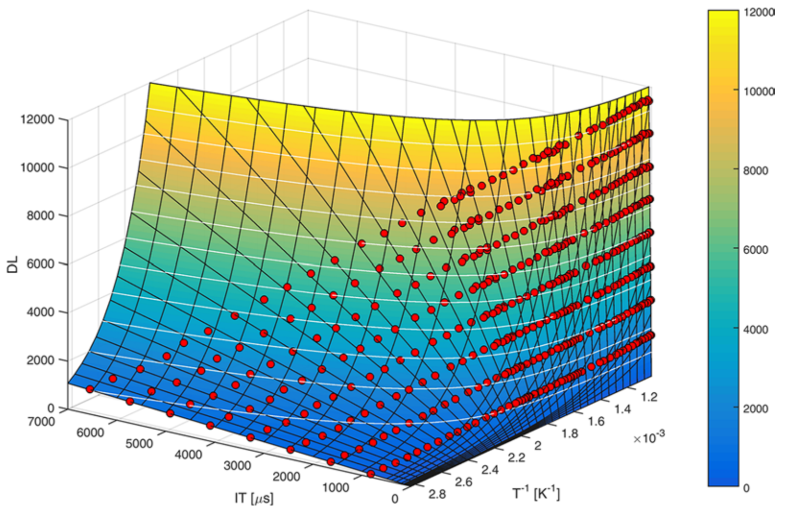

Figure 8. Calibration of the optical drivetrain with the 3.63 μm CWL filter. Red circles represent experimental measurements: eight IT for every radiation level (or temperature). Constant DL contour lines are in white. The surface, fitted to the points using a model discussed in section 6, aims to illustrate the 3D trends within the data. IT gridline density is increased for low IT to better visualize the large gradients at lower values of T^{-1}.

Based on the trends observed in figure 9, a more complex piecewise (connected-by-dot) function was also considered:

$$P(R) = \begin{cases} A_0 & R \leqslant R_0 \\ A_1 + R \cdot (A_0 - A_1)/R_0 & R > R_0, \end{cases} \tag{8}$$

where R_0 is the value of radiation where a transition between the constant and the linear segments occurs.

Furthermore, inspired by the field of chemical photography, where Schwarzschild's equation was improved by the Kron–Halm equation [16], a hyperbolic function was another candidate that could be used to represent the data. As such, the following smooth and monotonously decreasing equation was considered:

$$P(R) = A_0 + 1 - \cosh(A_1 \cdot R). \tag{9}$$

The various $P(R)$ curves corresponding to equations with a power law dependence of IT are charted in figure 9.

The 2nd group consisted of polynomials in R, IT and $R \cdot IT$, such as:

$$DL = \sum_{i=1}^{n} A_i (R \cdot IT)^i; \quad DL = IT \cdot \sum_{i=1}^{n} A_i R^i + IT^2 \cdot \sum_{i=1}^{m} A_i R^i;$$
$$DL = R \cdot \sum_{i=1}^{n} A_i IT^i, \tag{10}$$

where A_i are fitting constants that vary amongst different equations.

The polynomial family of models included a quadratic equation with respect to $R \cdot IT$ (as suggested in [17], with $A_0 = 0$), and two additional models with higher order terms, shown in equations, respectively:

$$DL = R \cdot IT - A_2 (R \cdot IT)^2, \tag{11}$$

$$DL = R \cdot IT + A_1 \cdot R \cdot IT^2, \tag{12}$$

$$DL = R \cdot IT + (A_1 \cdot R + A_2 \cdot R^2 + A_3 \cdot R^3) \cdot IT^2. \tag{13}$$

The accuracy of models constructed based on the 2 different types of templates, (6) to (9) and (11) to (13), alongside the simple Schwarzschild equation, (2), was then compared. Fitting the 3D (IT, T, DL) data with the models was performed using MATLAB's Curve Fitting Tool ('cftool'), which solves the nonlinear problems using a least-squares scheme with robust regression using a bisquare weighting function. The various models and their appropriate *goodness-of-fit* (GOF) values, consisting of the *sum of square errors* (SSE) and *root mean square error* (RMSE), are summarized in table 2.

As can be seen from the GOF information presented in table 2, even the relatively simple Schwarzschild model (2) provides an improved fit (smaller SSE and RMSE) over the reciprocity law (equation (1)). In the case where radiations on the object do not differ significantly from calibration, or when computation time is more important than accuracy, one can use the Schwarzschild model (i.e. equation (2) with constant P) since it is analytically invertible and therefore results in a much faster computation. Furthermore, the GOF of the 1st group of equations, (6)–(9), is generally superior to that of the 2nd group, (11)–(13). For this reason, equations of the 2nd group are not considered any further. Among the 1st group, the parabolic power law correction of reciprocity, equation (7), provides a good fit across all filters.

7. Radiation estimates absent of prior calibration

In order for the nonlinearity correction to be applicable, multi-*IT* measurements have to be performed. The prior described method requires a full calibration where the incoming radiation, as well as the camera integration time, are independently varied in a controlled manner. Therefore, during experiments, a single-*IT* measurement is sufficient to obtain a corrected radiation value. Moreover, when used to process a measurement dataset, it enables converting the digital units into absolute physical quantity of radiation (or equivalent blackbody temperature).

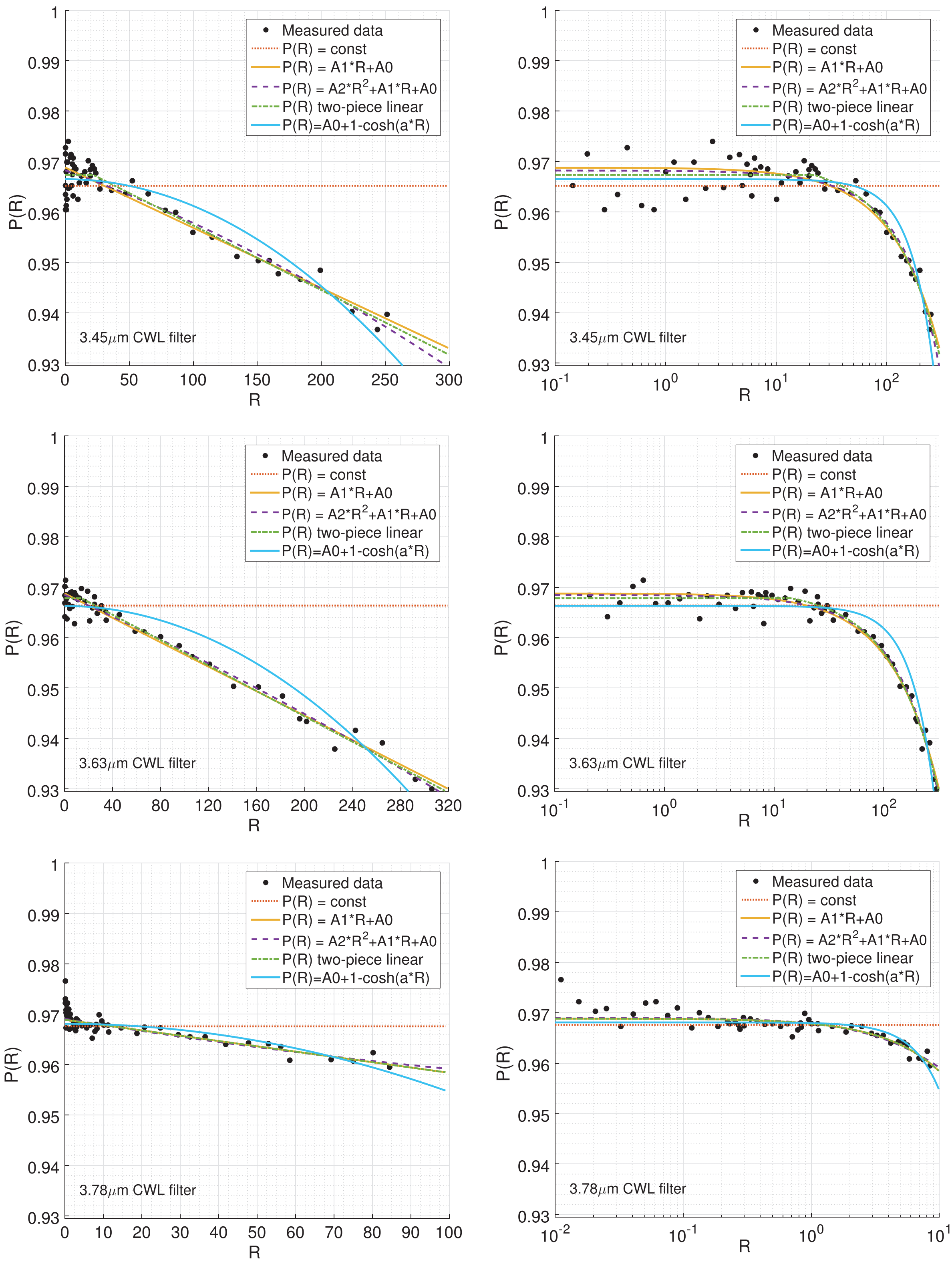

Figure 9. Illustrations of different models for the radiation dependence of the fitted power according to equation (5), for observations obtained using all three filters. Linear radiation scale (left) and logarithmic radiation scale (right). The coefficients A_0, A_1 and A_2 are different in each fit.

Alternatively, if multi-*IT* blackbody calibration does not exist, it is possible to demonstrate that the resulting nonlinearity can be corrected, as long as the incoming irradiation is steady (albeit unknown). Therefore, during the experiments, multi-*IT* data has to be acquired in order to correct for the nonlinearity effects. This yields radiation magnitude information in a relative sense through a post hoc analysis of preexisting data sets. For example, such a method may be useful when the desirable quantity consists of effective-emissivity ratios on a uniform temperature object.

Table 2. Goodness-of-fit comparison for different models. Model (1) is the baseline for comparison, and represents the fitting result obtained under the reciprocity assumption.

		3.45 μm CWL		3.63 μm CWL		3.78 μm CWL	
Equation	Mathematical expression	SSE	RMSE	SSE	RMSE	SSE	RMSE
(1)	$DL = R \cdot IT$	6.17E + 06	120.1	6.20E + 06	120.3	2.66E + 06	79.5
(2)	$DL = R \cdot IT^{A_0}$ (Schwarzschild's law)	1.52E + 06	59.6	1.54E + 06	60.1	4.92E + 05	34.2
(6)	$DL = R \cdot IT^{A_0 + A_1 \cdot R}$	1.55E + 06	60.3	1.55E + 06	60.2	4.05E + 05	31.1
(7)	$DL = R \cdot IT^{A_0 + A_1 \cdot R + A_2 \cdot R^2}$	9.83E + 05	48.0	9.35E + 05	46.8	1.75E + 05	20.4
(8)	$DL = R \cdot IT^{P(R)}$ where $P(R)$ is: $P(R) = \begin{cases} A_0 & R \leqslant R_0 \\ A_1 + R \cdot (A_0 - A_1)/R_0 & R > R_0 \end{cases}$	1.58E + 06	60.9	1.48E + 06	58.9	4.48E + 05	32.7
(9)	$DL = R \cdot IT^{A_0 + 1 - \cosh(A_1 \cdot R)}$	9.43E + 05	47.0	5.88E + 08	1173.3	2.64E + 06	79.3
(11)	$DL = R \cdot IT + A_2 \cdot (R \cdot IT)^2$	2.55E + 06	77.2	2.31E + 06	73.5	1.04E + 06	49.8
(12)	$DL = R \cdot IT + A_2 \cdot R \cdot IT^2$	6.14E + 06	119.8	6.18E + 06	120.2	1.68E + 06	63.2
(13)	$DL = R \cdot IT + (A_1 \cdot R + A_2 \cdot R^2 + A_3 \cdot R^3) \cdot IT^2$	2.39E + 06	75.0	2.02E + 06	69.0	9.85E + 05	48.6

7.1. Procedure for obtaining relative radiation estimates

The implementation of the alternative method reduces to one main task—obtaining an appropriate $P(R)$ function, such that equation (5) fits the experimental data well. In most applications, the observed scene may consist of multiple regions, each with its own radiation level. This can be attributed to their temperature, emissivity, relative angle and distance. Such a scenario inherently requires performing data acquisition with several different integration times due to various sensor dynamic ranges needed to measure both weak and intense radiations.

Observing equation (5) and the models in table 2, it is evident that R and the A_i coefficients that define $P(R)$ are initially unknowns for each experimental data point (represented by a DL and IT pair). The mathematical procedure therefore consists of obtaining estimates of R (potentially different for each point) and A_i, which are common for all points.

To get an initial approximation of R, each uniform-DL region undergoes a procedure where DL: $y_{DL} = [DL_1 \;\; DL_2 \;\; \dots \;\; DL_N]$ versus IT data: $x_{IT} = [IT_1 \;\; IT_2 \;\; \dots \;\; IT_N]$ are fitted by a power law relation. At each uniform-radiation region equation (5) degenerates into equation (2), in which R and P are constant. This method is repeated for each of the N different radiation regions, which results in their own local pairs of R_k and P_k, where $k = 1 \dots N$. This allows finding two relations: $P(R)$ and $DL(R, IT)$, using curve and surface fitting, respectively. A result of this scenario is demonstrated in figure 10, where two iso-R datasets (red points) and the fitted $DL(R, T)$ surface can be seen. The gridlines are iso-R and iso-IT curves, and the color of the surface represents iso-DL. After A_i are found, the relative radiation of any intermediate point may be computed using the numeric solution of equation (5). Thereby, the resulting radiation intensities are represented by comparable relative units.

7.2. Exemplary radiation correction

As demonstrated in figure 5, the calculations conducted under the reciprocity assumption led to imprecise results: radiations calculated from points acquired at different IT were unequal, even though R was constant in the experiment. The raw experimental data obtained from the setup of figure 3 are presented in table 3. Here, the data were used to demonstrate the correction procedure. The cavity and the metal were regarded as two regions of the scene with highly different levels of R. The correction was carried out as described in section 7.2. MATLAB's cftool was used for curve fitting. The correction results are summarized in table 4 and charted in figure 5 (red squares):

8. Nonlinearity of total exposure error implications in single band IR thermography

In this section, a conceptual temperature measurement experiment with an IR camera is considered. The example demonstrates the inaccuracies in single-band temperature estimates, which are associated with experimental data being processed under the invalid assumption of reciprocity. In this virtual experiment, an attempt is made to reproduce the temperature (T) from radiometric measurements (DL and IT pairs) for a range of target emissivities (ε). Since converting a given radiation level into temperature requires a calibration procedure to have been performed—real calibration data for the optical system (as shown in figure 8) are utilized. The temperature is estimated under the assumption of reciprocity (even though it does not hold), which highlights the resulting error.

Let an experimental scenario be such that both the calibration and the measurement are conducted at IT which result in mean DL value of 11,000 across the surface. This is within the system's extended dynamic range. Equation (7) is selected as a good representation of the real $P(R)$ behavior. The A_i parameters obtained from calibration data for the CWL = 3.45 μm filter are: $A_0 = 0.9621$, $A_1 = -2.871\text{E} - 6$ and $A_2 = -4.303\text{E} - 7$.

The radiation from a surface with emissivity $\varepsilon < 1$ is weaker compared to a blackbody of the same temperature. Therefore, in order to reach the same target DL, IT should be increased. The reciprocity assumption provides a way to

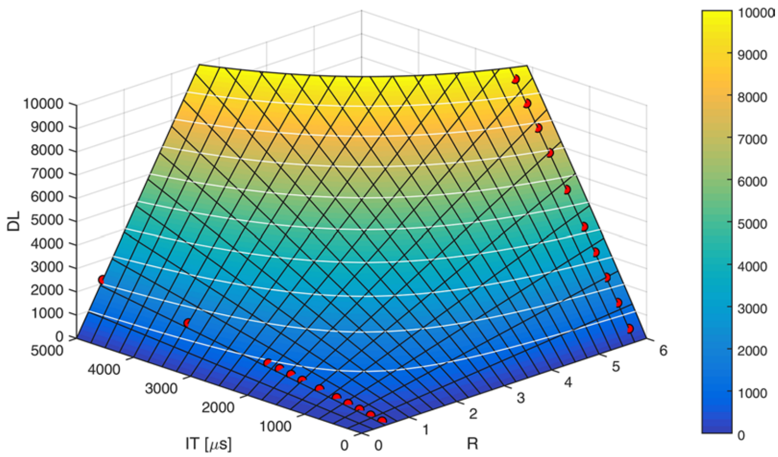

Figure 10. The surface fitting stage of the algorithm, for the 3.45 μm CWL filter. Measured points are displayed as red circles. Constant DL contour lines are in white.

Table 3. Raw experimental data for demonstration.

CWL 3.453			CWL 3.626			CWL 3.781		
IT	DL_{High}	DL_{Low}	IT	DL_{High}	DL_{Low}	IT	DL_{High}	DL_{Low}
100	501	49	100	643	63	100	233	21
300	1452	140	400	2465	240	300	675	59
500	2381	229	700	4247	413	600	1321	116
700	3305	317	1000	5997	583	900	1961	172
900	4220	404	1150	6870	668	1200	2594	227
1200	5574	534	1300	7735	753	1600	3430	300
1500	6918	665	1330	7914	770	2000	4253	373
1700	7814	752	1600	9467	922	2500	5284	463
1900	8706	837	3000	—	1688	2900	6104	534
2100	9590	921	3600	—	2018	3200	6716	586
3500	—	1506	4500	—	2511	5000	—	907
5000	—	2136	5500	—	3052	5800	—	1050

Table 4. Fit results and goodness-of-fit information for the demonstrational experimental data. *R* and *P* were obtained from MATLAB's cftool with the following options: fittype—'power1', 'Method'—'NonlinearLeastSquares', 'Robust'—'Bisquare'.

Filter	ε	R	P	SSE	RMSE
CWL 3.453	High	5.747 ± 0.035	0.9700 ± 0.0008	43.21	2.324
	Low	0.5537 ± 0.076	0.9696 ± 0.0016	16.17	1.272
CWL 3.626	High	7.362 ± 0.067	0.9704 ± 0.0012	39.41	2.563
	Low	0.717 ± 0.071	0.9702 ± 0.0012	16.6	1.289
CWL 3.781	High	2.664 ± 0.021	0.9705 ± 0.0010	31.47	1.984
	Low	0.2336 ± 0.022	0.9703 ± 0.0016	3.494	0.5911

compensate for the decrease in radiation intensity by a factor of ε; multiplying *IT* with $\varepsilon^{-1:}$

$$R_{GB} = R_{BB} \cdot \varepsilon \;\;\Rightarrow\;\; IT_{GB} = IT_{BB} \cdot \varepsilon^{-1} \tag{14}$$

$$DL_{target} = (R \cdot IT)_{GB} = (\varepsilon \cdot R_{BB}) \cdot (IT_{BB} \cdot \varepsilon^{-1}) = (R \cdot IT)_{BB}, \tag{15}$$

where the subscripts 'BB' and 'GB' signify 'blackbody' and 'greybody', respectively. Within this assumption, the effects of reduced radiation and prolonged *IT* cancel out, and the same target *DL* is maintained, equation (15).

Let the measured target object be a gray surface with temperature $t = 400$ °C and a known emissivity of $\varepsilon = 0.7$. During calibration, for a blackbody of this temperature, the IT_{BB} required to reach the target *DL* of 11 000 was 426.6 μs. Solving equation (7) for $(DL, IT_{BB}) = (11\,000, 426.6)$ yields $R_{BB} = 32.45$ [arb. units] with $P(R_{BB}) = 0.9621$. A model for integration time nonlinearity allows finding IT_{GB} that would be required in the experiment to get the target *DL* for such a surface:

$$IT_{GB} = (DL_{target}/\varepsilon R_{BB})^{P(\varepsilon R_{BB})^{-1}} = \left({}^{11000}\!\big/_{0.7 \cdot 32.45}\right)^{1.0394} \approx 618\ \mu\text{s}. \tag{16}$$

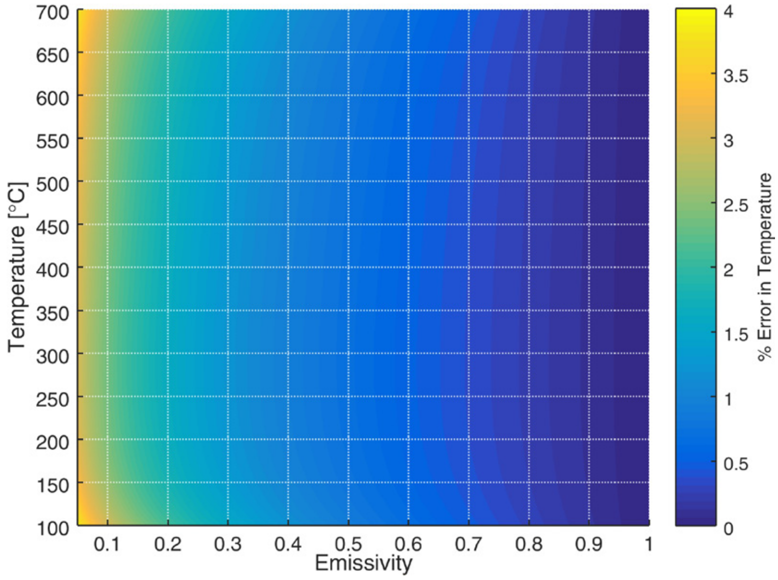

Figure 11. The error (%) resulting from assuming reciprocity for different emissivity (0.05–1) and temperature (100–700 °C) combinations based on calibration data for the 3.45 μm CWL filter.

Table 5. Contributions of the camera and the blackbody to the calibration uncertainty.

Source	Description	Documented uncertainty
Blackbody	Thermocouple accuracy	$\pm$1.75 °C or better for $T \leqslant 750$ °C; 95.5%
	Temperature stability	$\pm$0.5 °C
	Temperature resolution	0.1 °C
	Emissivity	0.99 ± 0.01
Camera	Detector electronic noise	4.74DL at 25 °C, IT = 2600 μs, $DL_{nominal} = 8373$. NETD $\approx$ 0.02 °C.

Under the reciprocity assumption, the IT_{BB} from equation (14) can be obtained by simple multiplication of IT_{GB} with emissivity, resulting in $IT_{BB} = 432.6$ μs. Evidently, IT_{BB} obtained using reciprocity is slightly higher than IT_{BB} encountered during calibration. Therefore, the apparent radiation flux is weaker than the expected one, which results in the underestimation of temperature. The relative error of DL resulting from the reciprocity assumption is expressed by:

$$\Delta_{DL} = \left| \frac{R \cdot IT - R \cdot IT^{P(R)}}{R \cdot IT^{P(R)}} \right| = \left| IT^{1-P(R)} - 1 \right|. \qquad (17)$$

It can be seen from equation (17) that for a constant R, the error associated with reciprocity, Δ_{DL}, increases with IT.

Since the calibration is performed at a constant target DL, there is an injective relation between IT_{BB} and T_{BB}; $IT_{BB} = 432.6$ μs corresponds to a blackbody at ~398.5 °C—a 0.37% error in temperature ($\Delta t = 1.5$ °C). If the emissivity of the body was instead 0.1, a case closer to polished metals, the computed temperature would be ~390.5 °C—with a larger error of 2.4% ($\Delta t = 9.5$ °C). Errors for other combinations of temperatures and emissivities are charted in figure 11. The slightly higher error around the extrema (~700 and ~100 °C) may be attributed to the fit being less accurate close to its edges; and to a very low SNR as a consequence of low emissivity, temperature, or a combination thereof.

9. Sources of calibration uncertainty

In the scope of this investigation, several working assumptions were made, which facilitate the characterization of the method uncertainty:

- Ambient radiation is negligible.
- Atmospheric absorption along the line-of-sight is negligible.
- The time difference between the object image acquisition and the corresponding background is sufficiently small for background subtraction to remove FPN.
- Non-uniformity of the ambient temperature throughout the calibration (which was conducted over a few days, several hours each day) does not affect the calibration's result.
- Temporal temperature changes in the ambiance, the optical elements, and the camera body are sufficiently slow to be negligible after background subtraction.

Sources of precision error in radiation thermometry can be associated with one of four things: the observed object, the transmission path, the measurement device and the data processing procedure. The uncertainty in the radiometric measurement of temperature of a gray body is obtained using equation (3) multiplied by ε:

$$R_{\text{measured}} \triangleq \varepsilon(\lambda, T) B_\lambda(\lambda, T) \Rightarrow B = R/\varepsilon, \qquad (18)$$

where the Planck distribution B, is replaced by the Wien approximation,

$$B_\lambda(\lambda,T)=\varepsilon(\lambda)\frac{c_1}{\lambda^5}\frac{1}{\exp(c_2/\lambda T)-1}\approx\varepsilon(\lambda)\frac{c_1}{\lambda^5}\exp(-c_2/\lambda T).$$

The propagated error is found using the variance formula:

$$\sigma_f(x,y)=\sqrt{\left(\frac{\partial f}{\partial x}\right)^2\sigma_x^2+\left(\frac{\partial f}{\partial y}\right)^2\sigma_y^2}, \tag{19}$$

which in the case of a fractional relation, as defined in equation (18), gives

$$\frac{\Delta B}{B}=\sqrt{\left(\frac{\Delta R}{R}\right)^2+\left(\frac{\Delta\varepsilon}{\varepsilon}\right)^2}. \tag{20}$$

The differential ΔB is expressed in terms of ΔT as follows

$$\Delta B=\frac{\Delta B}{\Delta T}\Delta T=\frac{\partial B}{\partial T}\Delta T. \tag{21}$$

Substituting equation (21) into the LHS of equation (20) results in

$$\frac{\Delta B}{B}=\frac{\partial B/\partial T}{B}\Delta T=\frac{c_2}{\lambda T^2}\Delta T. \tag{22}$$

This finally yields an expression for the temperature error:

$$\Delta T=\frac{\lambda T^2}{c_2}\sqrt{\left(\frac{\Delta R}{R}\right)^2+\left(\frac{\Delta\varepsilon}{\varepsilon}\right)^2}. \tag{23}$$

For a typical wavelength of $\lambda = 3.63$ μm at a temperature of $t = 25$ °C equation (23) amounts to ± 0.227 °C, and for $t = 700$ °C $\pm$ 2.42 °C. It can be seen that the contribution of radiation and emissivity error to temperature uncertainty increases with wavelength and with the square of temperature.

Consisting of both the bias and random errors, the computed total temperature uncertainty of less than 0.3% assumes that total exposure non-linearity has been properly compensated. If not, with the systematic temperature error of up to 4%, the nonlinearity effect can be more than an order of magnitude larger than any of the other contributing factors.

10. Summary and conclusions

While attempting to conduct radiometric measurements with an IR camera, low precision was encountered in subsequent acquisitions at multiple integration times (multi-*IT*). The cause of the imprecision was hypothesized, and later confirmed, to be associated with the failure of the reciprocity law. A comprehensive calibration of the camera using a blackbody source was conducted, which included scans over different combinations of temperature and integration time. A nonlinearity of the total exposure (NTE) was documented; it consists of integration nonlinearity (deviation of the output signal from a straight line, when observing a constant radiation flux at different exposure times) and reciprocity failure (deviation from a constant integrated signal, when varying the flux and inversely adapting the exposure time).

The aggregate error associated with NTE was found to be larger when long integration times were used, or when low emissivity surfaces were observed. Various equations were considered to model this phenomenon, and a large dataset was used to select the most appropriate empirical equation. The form that best compensates for NTE was found to be a radiation-dependent power law.

Two correction methods were proposed in this work, which rely on multi-*IT* data. The first method fulfills this requirement inherently by having multi-*IT* calibration data available for a known radiation source; and therefore, a measurement at a single integration time is sufficient to obtain a corrected radiation value. This method also enables quantitative measurement of radiation. The second method, absent of the prior multi-*IT* calibration, instead mandates multi-*IT* datasets to be taken during the experiment, which results in an internally consistent scale to compare different radiation intensities.

NTE compensation was determined to be essential for precise and consistent estimates of the incident radiation across different choices of integration time. The error implications on commonly employed single band temperature measurements were estimated to be 2.4% of the measured value.

In conclusion, failure of the reciprocity law was experimentally demonstrated in a semiconductor camera within the mid-wave IR spectrum for typically encountered radiation levels and integration time values. To our knowledge, this is the first effort that fully characterizes and corrects for the nonlinearity of total exposure in MWIR cameras.

References

[1] Anderson W 1987 Probabilistic models of the photographic process *Advances in the Statistical Sciences: Applied Probability, Stochastic Processes, and Sampling Theory* (Berlin: Springer) pp 9–40

[2] Martin J W, Chin J W and Nguyen T 2003 Reciprocity law experiments in polymeric photodegradation: a critical review *Prog. Org. Coat.* **47** 292–311

[3] Biesiadzinski T, Lorenzon W, Newman R, Schubnell M, Tarlé G and Weaverdyck C 2011 Reciprocity failure in HgCdTe detectors: measurements and mitigation *Publ. Astron. Soc. Pac.* **123** 958–63

[4] Biesiadzinski T, Lorenzon W, Schubnell M, Tarlé G and Weaverdyck C 2014 NIR detector nonlinearity and quantum efficiency *Publ. Astron. Soc. Pac.* **126** 243–9

[5] Pacheco-Labrador J, Ferrero A and Martín M P 2014 Characterizing integration time and gray-level-related nonlinearities in a NMOS sensor *Appl. Opt.* **53** 7778–86

[6] Smith R M, Zavodny M, Rahmer G and Bonati M 2008 A theory for image persistence in HgCdTe photodiodes *Proc. SPIE* **7021** 70210J

[7] Perry D L and Dereniak E L 1993 Linear theory of nonuniformity correction in infrared staring sensors *Opt. Eng.* **32** 1854–9

[8] Schulz M J and Caldwell L V 1995 Nonuniformity correction and correctability of infrared focal plane arrays *Proc. SPIE* **2470** 210050

[9] Ochs M, Horbach T, Schulz A, Koch R and Bauer H 2009 A novel calibration method for an infrared thermography system applied to heat transfer experiments *Meas. Sci. Technol.* **20** 075103

[10] Ferrero A, López M, Campos J and Sperling A 2014 Spatial characterization of cameras for low-uncertainty radiometric measurements *Metrologia* **51** 316
[11] Mangoubi S and Naveh O 2012 Non-uniformity correction of images generated by focal plane arrays of photodetectors *US Patent Specification* US8319862 B2
[12] Toczek T, Hamdi F, Heyrman B, Dubois J, Miteran J and Ginhac D 2013 Scene-based non-uniformity correction: from algorithm to implementation on a smart camera *J. Syst. Archit.* **59** 833–46
[13] Berrebi S 2008 DP004U-B: Calibration Procedure, FLIR Systems
[14] Nesher O *et al* 2003 Digital cooled InSb detector for IR detection *Proc. SPIE* **5074** 498154
[15] Vollmer M and Möllmann K-P 2010 *Infrared Thermal Imaging: Fundamentals, Research and Applications* (New York: Wiley)
[16] Halm J K E 1915 Determination of fundamental photographic magnitudes *Mon. Not. R. Astron. Soc.* **75** 150–77
[17] Kubik B, Barbier R, Castera A, Chabanat E, Ferriol S and Smadja G 2014 Impact of noise covariance and nonlinearities in NIR H2RG detectors *Proc. SPIE* **9154** 91541Q